



Title: A new  $(\text{Mg}_{0.5}\text{Fe}^{3+}_{0.5})(\text{Si}_{0.5}\text{Al}^{3+}_{0.5})\text{O}_3$   $\text{LiNbO}_3$ -type phase synthesized at lower mantle conditions  
Author: Zhaodong Liu, Leonid Dubrovinsky, Catherine McCammon, Sergey V. Ovsyannikov, Iuliia Koemets, Luyao Chen, Qi Cui, Na Su, Jinguang Cheng, Tian Cui, Bingbing Liu, Tomoo Katsura  
Publication: American Mineralogist  
Publisher: Mineralogical Society of America  
Date: online on 01 August 2019

This is the peer reviewed version of the following article: [Zhaodong Liu, Leonid Dubrovinsky, Catherine McCammon, Sergey V. Ovsyannikov, Iuliia Koemets, Luyao Chen, Qi Cui, Na Su, Jinguang Cheng, Tian Cui, Bingbing Liu, Tomoo Katsura (2019) A new  $(\text{Mg}_{0.5}\text{Fe}^{3+}_{0.5})(\text{Si}_{0.5}\text{Al}^{3+}_{0.5})\text{O}_3$   $\text{LiNbO}_3$ -type phase synthesized at lower mantle conditions. American Mineralogist, 104 (8): 1213–1216], which has been published in final form at <https://doi.org/10.2138/am-2019-7070>. This article may be used for non-commercial purposes in accordance with Mineralogical Society of America Terms and Conditions for Use of Self-Archived Versions.

1 **A new  $(\text{Mg}_{0.5}\text{Fe}^{3+}_{0.5})(\text{Si}_{0.5}\text{Al}^{3+}_{0.5})\text{O}_3$  LiNbO<sub>3</sub>-type phase synthesized at lower**  
2 **mantle conditions**

3 Zhaodong Liu<sup>1, 2 \*</sup>, Leonid Dubrovinsky<sup>1</sup>, Catherine McCammon<sup>1</sup>, Sergey V. Ovsyannikov<sup>1</sup>,  
4 Iuliia Koemets<sup>1</sup>, Luyao Chen<sup>2</sup>, Qi Cui<sup>3</sup>, Na Su<sup>3</sup>, Jinguang Cheng<sup>3, 4</sup>, Tian Cui<sup>2</sup>, Bingbing Liu<sup>2</sup>,  
5 Tomoo Katsura<sup>1, 5</sup>

6 <sup>1</sup>Bayerisches Geoinstitut, University of Bayreuth, Bayreuth 95440, Germany.

7 <sup>2</sup>State Key Laboratory of Superhard Materials, Jilin University, Changchun 130012, China

8 <sup>3</sup>Beijing National Laboratory for Condensed Matter Physics and Institute of Physics, Chinese Academy of  
9 Sciences, Beijing 100190, China.

10 <sup>4</sup>Songshan Lake Materials Laboratory, Dongguan, Guangdong 523808, China.

11 <sup>5</sup>Center for High Pressure Science and Technology Advanced Research, Beijing, 100094, P.R. China

12 \* Corresponding author: Zhaodong Liu ([liu\\_zhaodong@jlu.edu.cn](mailto:liu_zhaodong@jlu.edu.cn))

13

14

15 **Abstract**

16 A new  $(\text{Mg}_{0.5}\text{Fe}^{3+}_{0.5})(\text{Si}_{0.5}\text{Al}^{3+}_{0.5})\text{O}_3$  LiNbO<sub>3</sub>-type phase was synthesized at 27 GPa and 2000 K  
17 under highly oxidized conditions using an advanced multi-anvil apparatus. Single crystals for  
18 this phase are 0.2-0.3 mm in dimension and maroon in color. They crystallize in a  
19 noncentrosymmetric structure with space group *R3c* and lattice parameters of  $a = b = 4.8720$  (6)  
20 Å,  $c = 12.898$  (2) Å, and  $V = 265.14$  (8) Å<sup>3</sup>. Fe<sup>3+</sup> and Al<sup>3+</sup> cations substitute into *A* (Mg<sup>2+</sup>) and *B*  
21 (Si<sup>4+</sup>) sites through charge-coupled substitution mechanism, respectively. The distortion of BO<sub>6</sub>  
22 ( $B = \text{Si}_{0.5}\text{Al}^{3+}_{0.5}$ ) octahedra is 1.6 times higher than that of AO<sub>6</sub> ( $A = \text{Mg}_{0.5}\text{Fe}^{3+}_{0.5}$ ) octahedra.  
23 This phase is probably recovered from bridgmanite at lower-mantle conditions by a diffusionless  
24 transition because of the displacement of A cations and distortion of BO<sub>6</sub> octahedra on releasing  
25 pressure. Bridgmanite can thus contain the FeAlO<sub>3</sub> component (50 mol%) beyond previously  
26 reported solubility limit (37 mol%). The present study shows that the Earth's most abundant  
27 elements form a new Fe<sup>3+</sup>- and Al<sup>3+</sup>-rich LiNbO<sub>3</sub>-type compound from bridgmanite at lower  
28 mantle conditions. This new compound provides a new insight into the complicated crystal  
29 chemistry of LiNbO<sub>3</sub>-type phase/bridgmanite and constrains the pressure and temperature  
30 conditions for shocked meteorites.

31 **Keywords:** LiNbO<sub>3</sub>-type, single crystals, bridgmanite, crystal chemistry, lower mantle

32

## 33 INTRODUCTION

34 Phase compositions of  $ABO_3$  compounds are of great significance in physics, chemistry, and  
35 geoscience. Among  $ABO_3$  compounds,  $LiNbO_3$  ( $LN$ )-type compounds exhibit remarkable  
36 physical properties because of their noncentrosymmetric structure (space group:  $R3c$ ) and  
37 capacity to adopt a multitude of distortions between  $BO_6$  and  $AO_6$  octahedra (Navrotsky et al.,  
38 1998). Some  $LN$ -type oxides such as  $LiNbO_3$  and  $LiTaO_3$  can be prepared at ambient conditions  
39 (Megaw, 1968; Abrahams and Bernstein, 1967), whereas the majority of  $LN$ -type oxides have been  
40 regarded as a metastable quench phase formed from high-pressure stable orthorhombic  
41 perovskite by a diffusionless transformation upon decompression (e.g., Ross et al., 1989;  
42 Leinenweber, 1991; Navrotsky et al., 1998; Ishii et al. 2017). Natural  $LN$ -type  $FeTiO_3$  was also  
43 discovered in shocked gneiss from the Ries impact crater, southern Germany (Dubrovinsky et al.,  
44 2009), and can be used an indicator for shock conditions (Akaogi et al., 2016). Consequently,  
45 synthesis of new  $LN$ -type compounds and exploration of the novel functionalities related to their  
46 structures are important in Earth and planetary science as well as physics and material science.

47  $MgSiO_3$  perovskite (bridgmanite) is one of the most common  $ABO_3$  phases in the Earth's  
48 mantle, and can contain a large amount of  $Fe^{3+}$  in the presence of  $Al^{3+}$  (McCammon, 1997; Frost  
49 and Langenhorst, 2002). The incorporation of  $Fe^{3+}$  and  $Al^{3+}$  would great change the physical and  
50 chemical properties of bridgmanite such as elasticity (e.g., Boffa Ballaran et al., 2012), electrical  
51 conductivity (e.g., Yoshino et al., 2016), and Mg-Fe partitioning in the lower-mantle phases  
52 (Frost and Langenhorst, 2002). Several studies have found that  $MgSiO_3$  bridgmanite with the  
53  $Al_2O_3$  contents above 25 mol% would transform to the  $LN$ -type phase upon releasing pressure  
54 (Funamori et al., 1997; Miyajima et al., 1999; Liu et al., 2016, 2017a; Ishii et al., 2017). The

55 presence of  $\text{Al}^{3+}$  can also enhance the incorporation of  $\text{Fe}^{3+}$  to form the charge-coupled  $\text{FeAlO}_3$   
56 component in bridgmanite through the following reaction:  $\text{Al}_2\text{O}_3 + 3\text{Fe}^{2+}\text{O} = 2\text{Fe}^{3+}\text{AlO}_3 + \text{Fe}^0$   
57 (Frost and Langenhorst, 2002). The effective ionic radius of  $\text{Fe}^{3+}$  (0.645 Å) in six-fold  
58 coordination is significantly larger than that of  $\text{Al}^{3+}$  (0.535 Å) and  $\text{Si}^{4+}$  (0.40 Å) but close to that  
59 of  $\text{Mg}^{2+}$  (0.72 Å) (Shannon, 1976). In principle,  $\text{Fe}^{3+}$  preferentially substitutes on the *A* ( $\text{Mg}^{2+}$ )  
60 site rather than the *B* ( $\text{Si}^{4+}$ ) site due to comparable cation sizes. It is thus expected that  $\text{FeAlO}_3$ -  
61 bearing *LN*-type phases can be synthesized at lower mantle conditions and exhibit similar or  
62 distinct physical and chemical properties with only Al-bearing *LN*-type phases. However, such  
63 issues remain poorly understood.

64 Here, we report a new *LN*-type compound  $(\text{Mg}_{0.5}\text{Fe}^{3+}_{0.5})(\text{Si}_{0.5}\text{Al}^{3+}_{0.5})\text{O}_3$  with *R3c*  
65 symmetry synthesized at 27 GPa and 2000 K in a multi-anvil press. We investigate the crystal  
66 structure of the *LN*-type phase by means of single crystal X-ray diffraction, electron probe  
67 microanalyzer, and Mössbauer spectroscopy. Finally, we discuss the crystal chemistry of the *LN*-  
68 type phase and its implications for the mineralogy of the lower mantle and the pressure and  
69 temperature conditions of shocked meteorites.

70

## 71 **EXPERIMENTAL METHODS**

72 A fine-grained oxide mixture with a bulk composition 50 mol%  $\text{MgSiO}_3$  plus 50 mol%  
73  $\text{FeAlO}_3$  was used as the starting material, which was prepared from reagent-grade oxide powders  
74 of  $\text{MgO}$ ,  $\text{SiO}_2$ ,  $\text{Al}_2\text{O}_3$ , and  $\text{Fe}_2\text{O}_3$  with a grain size smaller than 1  $\mu\text{m}$ . The starting material was  
75 loaded into a platinum capsule, heated at 800 K for one hour, and then welded. This procedure is  
76 expected to maintain  $\text{Fe}^{3+}/\sum\text{Fe} = 100\%$  and minimize absorbed water. Quench experiments were

77 performed at 27 GPa and 2000 K for 20 hours using a Cr<sub>2</sub>O<sub>3</sub>-doped MgO octahedron with a 7-  
78 mm edge length and LaCrO<sub>3</sub> sleeve for heating in combination with tungsten carbide cubes with  
79 3-mm truncated edge lengths in a Kawai-type multi-anvil apparatus (IRIS-15) with a press load  
80 of 15 MN at the Bayerisches Geoinstitut, University of Bayreuth (Ishii et al., 2016; Liu et al.  
81 2017b).

82 Phases in recovered samples were initially identified using a micro-focused X-ray  
83 diffraction (MXRD) with a Co anode operated at 40 kV and 500 mA. Back-scattered electron  
84 (BSE) images were obtained using a LEO1530 scanning electron microscope (SEM). Phase  
85 compositions were analyzed using a JEOL JXA-8200 electron probe microanalyzer (EPMA)  
86 operating at an acceleration voltage of 15 kV and a beam current of 5 nA with standards of  
87 enstatite for Mg and Si and corundum for Al. A high-quality single crystal of ~0.04 mm in  
88 diameter was selected for single crystal X-ray diffraction (SXRD) and the data were collected at  
89 ambient conditions using a three-circle diffractometer equipped with a SMART APEX CCD  
90 detector and a high-brilliance I $\mu$ s 3.0 microfocus anode (Ag radiation). The exposure time was  
91 10 s per frame. Lorentz and polarization corrections as well as an analytical absorption  
92 correction based on the crystal shape were taken into account for the correction of the reflection  
93 intensities using the CrysAlis package (Oxford Diffraction 2017). All crystallographic data  
94 refinements were performed based on  $F^2$  using the SHELX97 program package (Sheldrick, 2008)  
95 in the WinGX System (Farrugia, 1999). The Fe<sup>3+</sup>/ $\Sigma$ Fe ratio was measured using Mössbauer  
96 spectroscopy on one the same single crystal, which was conducted in transmission mode on a  
97 constant acceleration Mössbauer spectrometer with a nominal 370 MBq <sup>57</sup>Co point source in a 12  
98 mm Rh matrix. The velocity scale was calibrated relative to  $\alpha$ -Fe. Detailed information can be  
99 found in McCammon (1994).

100

## 101 RESULTS AND DISCUSSIONS

102 The MXRD pattern of the recovered sample indicates that all diffraction peaks can be  
103 matched to those of an *LN*-type phase (Fig. 1a). A BSE image further confirms that the run  
104 product consists of only a single phase with grain sizes on the order of 0.2-0.3  $\mu\text{m}$  (Fig. 1b).  
105 Optical microscope observations show that the crystals are translucent, maroon in color, and free  
106 of visible imperfections (Fig. 1c). The room temperature Mössbauer spectrum of the sample (Fig.  
107 1d) can be fit to one doublet. The hyperfine parameters, center shift (CS) and quadruple splitting  
108 (QS), are  $0.34 \pm 0.01$  and  $0.91 \pm 0.01$  mm/s, respectively. These values are in good agreement  
109 with  $\text{Fe}^{3+}$  in silicate perovskite with CS of  $\sim 0.3$  mm/s and QS of 0.73–0.94 mm/s (McCammon,  
110 1997; Lauterbach et al. 2000). However, a doublet with high CS and QS characteristic of  $\text{Fe}^{2+}$  in  
111 silicate perovskite is not observed. The  $\text{Fe}^{3+}/\Sigma\text{Fe}$  value is thus 100% within analytical uncertainty,  
112 suggesting a pure  $\text{Fe}^{3+}$ -bearing *LN* phase. EPMA shows that the *LN*-type phase has a  
113 composition of  $(\text{Mg}_{0.49 \pm 0.01}\text{Fe}^{3+}_{0.49 \pm 0.01}\text{Al}^{3+}_{0.02 \pm 0.01})(\text{Si}_{0.50 \pm 0.01}\text{Al}^{3+}_{0.50 \pm 0.01})\text{O}_{3.01 \pm 0.01}$ . Because  
114 the effective ionic radius of  $\text{Fe}^{3+}$  (0.645 Å) in six-fold coordination is closer to that of  $\text{Mg}^{2+}$  (0.72  
115 Å) rather than to that of  $\text{Si}^{4+}$  (0.40 Å), and the radius of  $\text{Al}^{3+}$  (0.535 Å) is closer to that of  $\text{Si}^{4+}$ ,  
116  $\text{Fe}^{3+}$ , and  $\text{Al}^{3+}$  are expected to substitute for  $\text{Mg}^{2+}$  (*A* site) and  $\text{Si}^{4+}$  (*B* site), respectively, through  
117 a charge-coupled substitution ( $\text{Fe}^{3+}(\text{A}) + \text{Al}^{3+}(\text{B}) = \text{Mg}^{2+}(\text{A}) + \text{Si}^{4+}(\text{B})$ ). But we note that a small  
118 fraction of  $\text{Al}^{3+}$  may be present on the *A* site (within the uncertainty of the measurements) due to  
119 an excess of Al. These results will be discussed below based on the results of SXRDR refinement.

120 Crystallographic data for the *LN*-type  $(\text{Mg}_{0.5}\text{Fe}^{3+}_{0.5})(\text{Si}_{0.5}\text{Al}^{3+}_{0.5})\text{O}_3$  phase from the SXRDR  
121 refinement can be found in the deposited CIF. The lattice parameters and volume are  $a = b =$   
122  $4.8720(6)$  Å,  $c = 12.898(2)$  Å, and  $V = 265.14(8)$  Å<sup>3</sup>, which are substantially larger than those

123 reported for the  $\text{Mg}_{0.75}\text{Al}_{0.5}\text{Si}_{0.75}\text{O}_3$  LN-type phase ( $a = b = 4.8194(3) \text{ \AA}$ ,  $c = 12.6885(8) \text{ \AA}$ ,  $V =$   
124  $255.23(3) \text{ \AA}^3$ ; Ishii et al., 2017). More than 900 unique reflections were collected and indexed in  
125 the space group  $R3c$  (#161) with  $R_{\text{int}} = 2.9\%$ . A structure solution based on the single crystal data  
126 was further refined in an anisotropic approximation for all atoms to  $R_1 = 5.9\%$ . The scattering  
127 factors of Mg, Al, and Si are similar, but very different to those of Fe. By assuming that both  
128 cation sites are fully occupied, we found that  $\text{Fe}^{3+}$  is located only in A site together with Mg.  
129 These results are in agreement with the Mössbauer spectroscopy data. Free refinement of the A-  
130 site occupancy yielded 0.48 (5) and 0.52 (5) for Mg and  $\text{Fe}^{3+}$ , respectively, which agrees with  
131 results of the chemical analysis. These two occupancies are indistinguishable from 0.5 within the  
132 uncertainties of this method. In the final structural refinement, we fixed the occupancies of  $\text{Fe}^{3+}$   
133 and Mg in the A-site to 0.5. Since Si and Al in the B site cannot be distinguished by SXRD, their  
134 occupancies were also fixed to 0.5 based on the composition.

135 As shown in Figure 2, the  $\text{Mg}_{0.5}\text{Fe}^{3+}_{0.5}$  and  $\text{Si}_{0.5}\text{Al}^{3+}_{0.5}$  atoms occupy six-coordinated A-  
136 and B-sites to form  $\text{AO}_6$  and  $\text{BO}_6$  octahedra, respectively, which are interpenetrated via edge-  
137 sharing octahedral dimers in the  $ab$ -plane and face-sharing octahedral pairs along the  $c$ -axis. The  
138 size of the  $\text{AO}_6$  octahedron ( $\sim 10.3 \text{ \AA}^3$ ) is significantly larger than that of the  $\text{BO}_6$  octahedron  
139 ( $\sim 8.6 \text{ \AA}^3$ ) because  $\text{AO}_6$  and  $\text{BO}_6$  octahedra are occupied by larger ( $\text{Mg}^{2+}$  and  $\text{Fe}^{3+}$ ) and smaller  
140 ( $\text{Si}^{4+}$  and  $\text{Al}^{3+}$ ) cations, respectively. Noticeable structural features include the distortions of  $\text{AO}_6$   
141 and  $\text{BO}_6$  octahedra as a result of shifts of A and B cations from the geometrical centers of face-  
142 sharing octahedra by 0.2 and 0.3  $\text{ \AA}$ , respectively (see deposited CIF). The average bond lengths  
143 of two types of  $\langle \text{Mg/Fe-O} \rangle$  are  $1.975 \pm 0.006$  and  $2.090 \pm 0.008 \text{ \AA}$ , which are significantly  
144 larger than those of  $\langle \text{Si/Al-O} \rangle$  ( $1.939 \pm 0.008$  and  $1.802 \pm 0.006 \text{ \AA}$ ). We estimated the  
145 octahedral distortion using the above bond lengths by the following equation:

146 
$$\Delta = \frac{1}{6} \sum_i \left\{ \frac{(d_i - d_{ave})}{d_{ave}} \right\}^2, \quad (1)$$

147 where  $d_i$  is the individual bond length and  $d_{ave}$  is the average bond length. Values of  $\Delta$  are  $8 \times 10^{-4}$   
 148 and  $13 \times 10^{-4}$  for  $(Mg_{0.5}Fe^{3+}_{0.5})O_6$  and  $(Si_{0.5}Al^{3+}_{0.5})O_6$  octahedra, respectively, confirming a  
 149 weaker distortion of  $AO_6$  than  $BO_6$ . Furthermore, the distortion of  $BO_6$  octahedra in the present  
 150 phase is significantly larger than that of  $MgSiO_3$  bridgmanite ( $1.6 \times 10^{-5}$ ) by a factor of 86.

151 We also use the Goldschmidt tolerance factor ( $t$ ) for  $LN$ -type or perovskite  $ABO_3$   
 152 compounds to express the geometric stability and crystal structure distortions in terms of  
 153 constituent ionic packing (Goldschmidt, 1926). The parameter  $t$  is defined by the ratios of  
 154 constituent ionic radii of  $A$ ,  $B$  and  $O$  as  $t = (r_A + r_O) / \sqrt{2}(r_B + r_O)$ , where  $r_A$ ,  $r_B$ , and  $r_O$  are  
 155 the ionic radii of  $A$  and  $B$  in six-fold coordination and  $O$ , respectively. As shown in Figure 3, we  
 156 obtained  $t = 0.79$  for  $(Mg_{0.5}Fe^{3+}_{0.5})(Si_{0.5}Al^{3+}_{0.5})O_3$  ( $r_{Mg^{2+}} = 0.72 \text{ \AA}$ ;  $r_{Al^{3+}} = 0.535 \text{ \AA}$ ;  $r_{Fe^{3+}} = 0.645$   
 157  $\text{ \AA}$ ;  $r_O = 1.4 \text{ \AA}$ ) in the present study, which is comparable with that of  $LN$ -type  $MnTiO_3$  ( $t = 0.79$ ,  
 158 Ross et al., 1989),  $Mg_{0.75}Al_{0.5}Si_{0.75}O_3$  ( $t = 0.80$ , Liu et al., 2016, 2017a; Ishii et al., 2017) but  
 159 significantly higher than that of  $FeTiO_3$  ( $t = 0.77$ , Leinenweber et al., 1991). All of these values  
 160 are significantly lower than those for stable perovskite of  $CaSiO_3$  ( $t = 0.95$ , Liu and Ringwood,  
 161 1975) and  $MgSiO_3$  ( $t = 0.83$ , Ito and Matsui, 1978). In summary,  $t$  decreases with increasing  $B$   
 162 cation radius relative to that of the  $A$  cation as a result of the increasing degree of cell distortion.

163

## 164 IMPLICATIONS

165 Most  $LN$ -type phases are generally accepted as a quenchable phase that back-transforms  
 166 from a high-pressure stable perovskite phase by a diffusionless transition because of the



167 displacement of A cations and distortion of  $\text{BO}_6$  octahedra resulting from cation substitution  
168 upon decompression (e.g., Navrotsky et al., 1998; Ross et al., 1989; Leinenweber, 1991; Ishii et  
169 al., 2017). It is noted that the charge-coupled  $\text{FeAlO}_3$  component dominates in bridgmanite,  
170 especially  $\text{Fe}^{3+}$ - and  $\text{Al}^{3+}$ -rich bridgmanite, although trace amounts of the oxygen vacancy  
171 substitution may exist in  $\text{Fe}^{3+}$ - and  $\text{Al}^{3+}$ -poor bridgmanite in the  $(\text{Mg}, \text{Fe}^{2+})\text{O}-\text{Fe}^{3+}\text{AlO}_3-\text{SiO}_2$   
172 ternary system (Fig. 4) (McCammon, 1997; Lauterbach et al. 2000; Frost and Langenhorst, 2002;  
173 Nishio-Hamane et al., 2005; Saikia et al., 2009; Boffa Ballaran et al. 2012; Yoshino et al., 2016).  
174 The  $\text{Al}_2\text{O}_3$  content (25 mol%) in the present phase is also considerably higher than that in the Fe-  
175 free bridgmanite (12 mol%, Liu et al., 2016; 2017a). Therefore, the  $\text{Al}_2\text{O}_3$  content in bridgmanite  
176 could be highly enhanced in the presence of  $\text{Fe}^{3+}$  because of the formation of the charge-coupled  
177  $\text{Fe}^{3+}\text{AlO}_3$  composition. In the present study, bridgmanite can incorporate the  $\text{FeAlO}_3$  content up  
178 to 50 mol% at 27 GPa and 2000 K, which is beyond solubility limit in both pyrolite (~6  
179 mol%) and MORB (mid-ocean ridge basalt) (~25 mol%) and previously reported value (37  
180 mol%, Boffa Ballaran et al., 2012). Bridgmanite would thus be the major phase for  $\text{Fe}^{3+}$  and  
181  $\text{Al}^{3+}$  for the pyrolite and MORB lower mantle.

182 Furthermore, the pressure at which the present phase forms (27 GPa) is significantly  
183 lower than that of the pyropic ( $\text{Mg}_3\text{Al}_2\text{Si}_3\text{O}_{12}$  pyrope) *LN*-type phase (45 GPa, Liu et al., 2016;  
184 2017a). This observation may be explained by a reduction of the ionic radius ratio between the  
185 A-site cation and oxygen because of the smaller  $\text{Fe}^{3+}$  in A (Mg) site and larger octahedral  
186 distortion than found in the pyropic *LN*-type phase. Our results together with that obtained by  
187 Boffa Ballaran et al. (2012) suggest that bridgmanite with the  $\text{FeAlO}_3$  content above ~37 mol%  
188 would transform into the *LN*-type phase upon decompression from lower mantle conditions.

189           The formation of the *LN*-type phase is a useful indicator for constraining the pressure and  
190 temperature conditions for shocked meteorites (Sharp et al., 1997; Xie et al., 2006; Tomioka and  
191 Fujino 1997; Ishii et al., 2016). Dubrovinsky et al. (2009) found a natural *LN*-type FeTiO<sub>3</sub> phase  
192 from the Ries Crater, Germany, which is considered to be recovered from perovskite at 15-28  
193 GPa after shocking (Akaogi et al., 2016). The presence of the Fe<sup>3+</sup>-and Al<sup>3+</sup>-rich *LN*-type phase  
194 can therefore be used to constrain the formation conditions of shocked meteorites.

195

## 196 **Acknowledgements**

197 The authors thank D. Krauß, H. Fischer, and S. Übelhack for their assistance with high-pressure  
198 assembly preparation. We also thanks for the editor Ian Swainson for processing our manuscript  
199 and four reviewers for constructive comments. Z. L. was financially supported by the  
200 Bayerisches Geoinstitut Visitors' Program. This study was also supported by research grants to T.  
201 K. (BMBF: 05K13WC2, 05K16WC2; DFG: KA3434/3-1, KA3434/7-1, KA3434/8-1,  
202 KA3434/9-1), L. D. (DU393/9-2, DU393/13-1), and C. M. (MC3/20-2). This project has  
203 received funding from the European Research Council (ERC) under the European Union's  
204 Horizon 2020 research and innovation programme (Proposal No. 787 527). J. G. C. is supported  
205 by the National Key R&D Program of China (Grant No. 2018YFA0305700), the National  
206 Science Foundation of China (Grant No. 11574377, 11874400), and the Key Research Program  
207 of Frontier Sciences (Grant No. QYZDB-SSWSLH013).

208

## 209 **References**

- 210 Abrahams, S. C., and Bernstein, J. L. (1967) Ferroelectric lithium tantalate—1. single crystal X-ray  
211 diffraction study at 24 C Journal of Physics and Chemistry of Solids, 28, 1685.
- 212 Akaogi, M., Abe, K., Yusa, H., Ishii, T., Tajima, T., Kojitani, H., Mori, D., and Inaguma, Y. (2016) High-  
213 pressure high-temperature phase relations in FeTiO<sub>3</sub> up to 35 GPa and 1600°C. Physics and  
214 Chemistry of Minerals, 44, 63–73.
- 215 Dubrovinsky, L.S., El Goresy, A., Gillet, P., Wu, X., and Simionivici, A. (2009) A novel natural shock-  
216 induced high-pressure polymorph of FeTiO<sub>3</sub> with the Liniobate structure from the Ries Crater,  
217 Germany. Meteoritics and Planetary Science Supplement, 72, 5094.
- 218 Frost, D. J., and Langenhorst, F., (2002) The effect of AlO<sub>1.5</sub> on Fe–Mg partitioning between  
219 magnesiowüstite and magnesium silicate perovskite. Earth and Planetary Science Letters, 199,  
220 227–241.
- 221 Funamori, N., Yagi, T., Miyajima, N., and Fujino, K. (1997) Transformation in garnet: from  
222 orthorhombic perovskite to LiNbO<sub>3</sub> phase on release of pressure. Science, 275, 513–515.
- 223 Goldschmidt, V. M. (1926) Naturwissenschaften, 14, 477.
- 224 Ishii, T., et al. (2016) Generation of pressure over 40 GPa using Kawai-type multi-anvil press with  
225 tungsten carbide anvils. Review of Scientific Instruments, 87, 024501–1–024501–6.
- 226 Ishii, T., Sinmyo, R., Komabayashi, T., Boffa-Ballaran, T., Kawazoe, T., Miyajima, N., and Katsura, T.  
227 (2017). Synthesis and crystal structure of LiNbO<sub>3</sub>-type Mg<sub>3</sub>Al<sub>2</sub>Si<sub>3</sub>O<sub>12</sub>: A possible indicator of shock  
228 conditions of meteorites. American Mineralogist, 102(9), 1947–1952.
- 229 Ito, E., and Matsui, Y. (1978) Synthesis and crystal–chemical characterization of MgSiO<sub>3</sub> perovskite.  
230 Earth and Planetary Science Letters, 38, 443–450.
- 231 Ko, J., and Prewitt, C. T. (1988) High-pressure phase transition in MnTiO<sub>3</sub> from the ilmenite to the  
232 LiNbO<sub>3</sub> structure. Physics and Chemistry of Minerals, 15, 355–362.
- 233 Lauterbach, S., McCammon, C. A., van Aken, P., Langenhorst, F., and Seifert, F., (2000) Mössbauer and  
234 ELNES spectroscopy of (Mg,Fe)(Si,Al)O<sub>3</sub> perovskite: a highly oxidised component of the lower  
235 mantle. Contributions to Mineralogy and Petrology, 138, 17–26.
- 236 Leinenweber, K., Utsumi, W., Tsuchida, Y., Yagi, T., and Kurita, K. (1991) Unquenchable high-pressure  
237 perovskite polymorphs of MnSnO<sub>3</sub> and FeTiO<sub>3</sub>. Physics and Chemistry of Minerals, 18, 244–250.

238 Liu, L., and A. E. Ringwood (1975) Synthesis of a perovskite-type polymorph of CaSiO<sub>3</sub>. Earth and  
239 Planetary Science Letter, **14**, 209–211.

240 Liu, Z. D., Irifune, T. Nishi. M., Tange, Y., Arimoto, and T., Shinmei, T. (2016) Phase relations in the  
241 system MgSiO<sub>3</sub>– Al<sub>2</sub>O<sub>3</sub> up to 52 GPa and 2000 K. Physics of the Earth and Planetary Interiors, 257,  
242 18–27.

243 Liu, Z. D., Nishi. M., Ishii, T., Fei, H. Z., Miyajima, N., Boffa Ballaran, T., Ohfuji, H., Sakai, T., Wang,  
244 L., Shcheka, S., Arimoto, T., Tange, Y., Higo, Y., Irifune, T., and Katsura, T. (2017a) Phase  
245 relations in the system MgSiO<sub>3</sub>–Al<sub>2</sub>O<sub>3</sub> up to 2300 K at lower-mantle pressures, Journal Geophysics  
246 Research, 10, 7775-7788.

247 Liu, Z. D., Ishii, T., and Katsura, T. (2017b) Rapid decrease of MgAlO<sub>2.5</sub> component in bridgmanite with  
248 pressure, Geochemical Perspective Letters, 5, 12-18.

249 McCammon, C.A. (1994) Mössbauer spectroscopy of quenched high-pressure phases: investigating the  
250 Earth's interior. Hyperfine Interact. 90, 89–105.

251 McCammon, C. A. (1997) Perovskite as a possible sink for ferric iron in the lower mantle. Nature, 387,  
252 694–696.

253 Megaw, H.D., 1968. A note on the structure of lithium niobate, LiNbO<sub>3</sub>. Acta Crystallographica A 24,  
254 583e588.

255 Miyajima, N., Fujino, K., Funamori, N., Kondo, T., and Yagi, T. (1999). Garnet-perovskite  
256 transformation under conditions of the Earth's lower mantle: An analytical transmission electron  
257 microscopy study. Physics of the Earth and Planetary Interiors, 116(1–4), 117–131.

258 Navrotsky, A. (1998) Energetics and crystal chemical systematic among ilmenite, lithium niobate, and  
259 perovskite structures. Chemistry of Materials 10, 2787e2793.

260 Nishio-Hamane, D., Nagai, T., Fujino, K., Seto, Y., and Takafuji, N. (2005) Fe<sup>3+</sup> and Al<sup>3+</sup> solubilities in  
261 MgSiO<sub>3</sub> perovskite: implication of the Fe<sup>3+</sup> AlO<sub>3</sub> substitution in MgSiO<sub>3</sub> perovskite at the lower  
262 mantle condition. Geophysical Research Letter, 32, L16306.

263 Oxford Diffraction. CrysAlisPro. Oxford Diffraction Ltd, Abingdon, Oxfordshire, 2009, UK.

264 Sheldrick, G. M. A short history of SHELX, Acta Crystallographica, 2008, A64, 112–122

265 Farrugia, L. J. (1999) WinGX suite for small-molecule single-crystal crystallography. Journal of Applied  
266 Crystallography.

267 Ross, N. L., Ko, J., and Prewitt, C.T. (1989) A new phase transition in  $\text{MnTiO}_3$ :  $\text{LiNbO}_3$ -perovskite  
268 structure. *Physics and Chemistry of Minerals*, 16, 621-629.

269 Saikia, A., Boffa Ballaran, T., and Frost, D.J., 2009. The effect of Fe and Al substitution on the  
270 compressibility of  $\text{MgSiO}_3$  perovskite determined through single-crystal X-ray diffraction. *Physics*  
271 *of the Earth and Planetary Interiors*, 173, 153–161.

272 Shannon, R.D. (1976) Revised effective ionic radii and systematic studies of interatomic distances in  
273 halides and chalcogenides. *Acta Crystallographica A*, 32, 751–767.

274 Sharp, T.G., Lingemann, C.M., Dupas, C., and Stöffler, D. (1997) Natural occurrence of  $\text{MgSiO}_3$ -ilmenite  
275 and evidence for  $\text{MgSiO}_3$ -perovskite in a shocked L chondrite. *Science*, 277, 352–355.

276 Tomioka, N. and Fujino, K. (1997) Natural  $(\text{Mg,Fe})\text{SiO}_3$ -ilmenite and-perovskite in the Tenham  
277 meteorite. *Science*, 277, 1084–1086.

278 Xie, Z., Sharp, T. G. and DeCarlie, P. S. (2006) High-pressure phases in a shock-induced melt vein of the  
279 Tenham L6 chondrite: Constraints on shock pressure and duration, *Geochimica et Cosmochimica*  
280 *Acta*, 70, 504–515.

281 Yoshino, T., kamada, S., Chengcheng, Z., Ohtani, E., and Hirao, N. (2016) Electrical conductivity model  
282 of Al-bearing bridgmanite with implications for the electrical structure of the Earth's lower mantle.  
283 *Earth and Planetary Science Letters*, 434, 208-219.

284

285

286

287

288

289

290

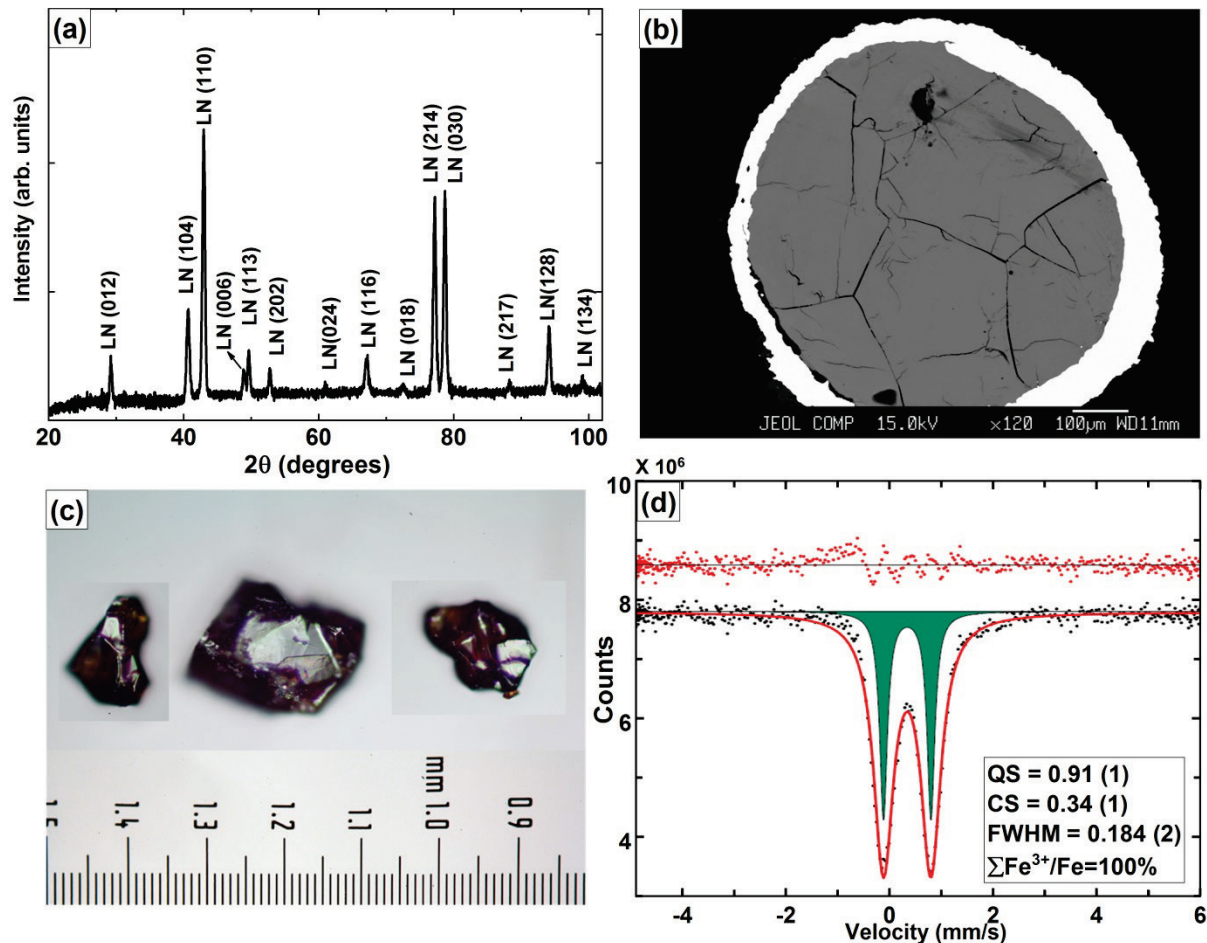
291

292

293

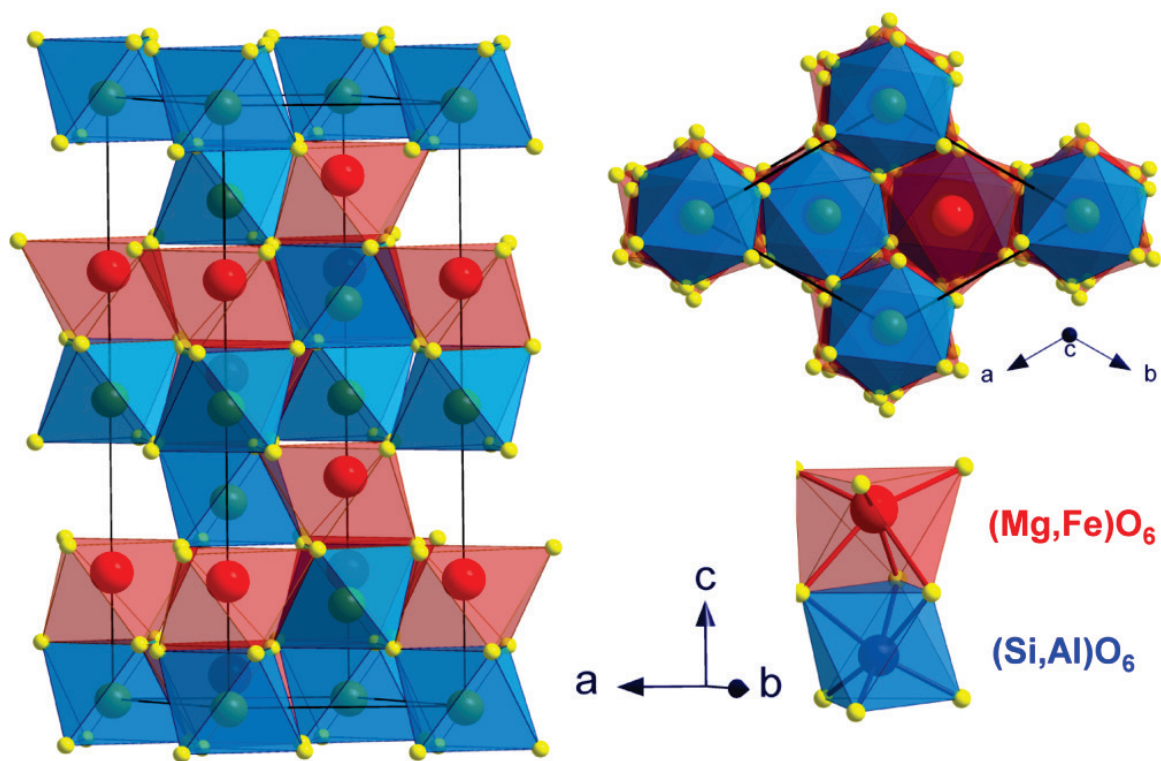
294

295

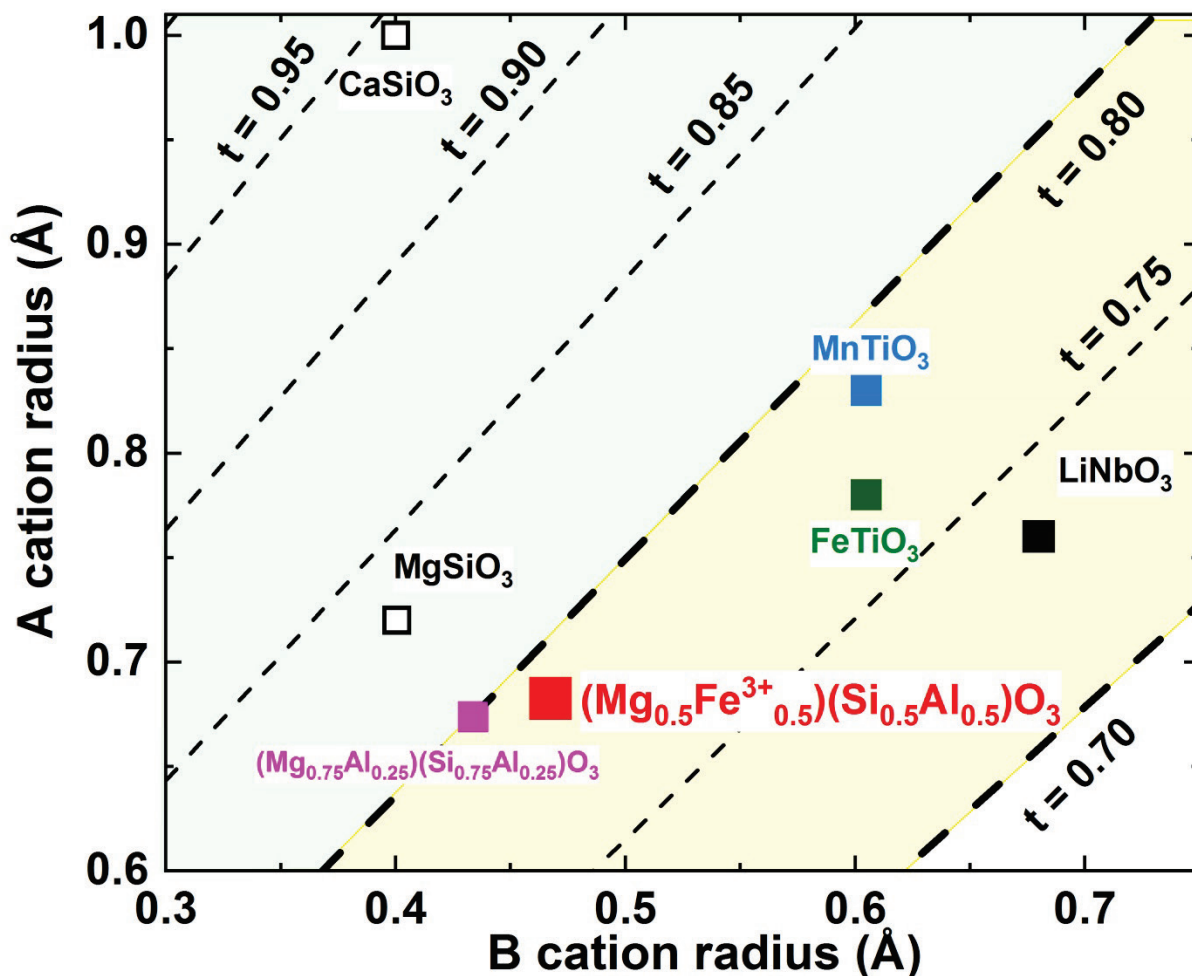


297

298 **FIGURE 1.** Characteristics of the  $(\text{Mg}_{0.5}\text{Fe}^{3+}_{0.5})(\text{Si}_{0.5}\text{Al}^{3+}_{0.5})\text{O}_3$  LN-type phase: (a) MXRD  
 299 profile, (b) BSE image, (c) photograph of selected single crystals, and (d) Mössbauer spectrum.  
 300 Black dots indicate experimental data, while the red line shows the fitted curve. Red dots  
 301 indicate the residual, i.e., the difference between calculated and experimental results. The small  
 302 deviations in the residual are likely due to slight deviation from Lorentzian lineshape due to  
 303 next-nearest-neighbor effects in the solid solution. Abbreviations: CS: center shift, QS:  
 304 quadruple splitting, FWHM: Full width at half maximum.



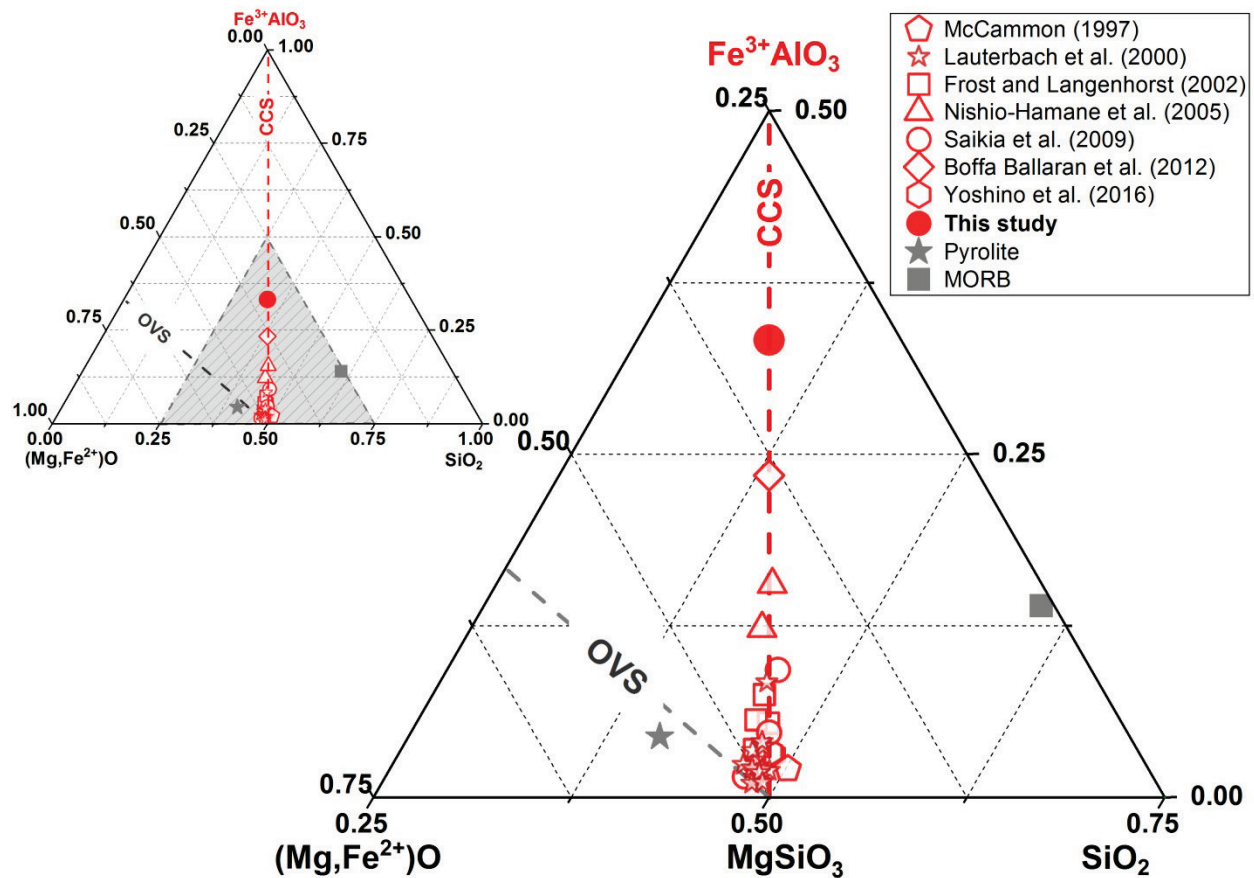
305  
 306 **FIGURE 2.** Crystal structure of the  $(\text{Mg}_{0.5}\text{Fe}^{3+}_{0.5})(\text{Si}_{0.5}\text{Al}^{3+}_{0.5})\text{O}_3$  LN-type phase and  $\text{AO}_6$  ( $A =$   
 307  $\text{Fe}^{3+}_{0.5}\text{Mg}_{0.5}$ ) and  $\text{BO}_6$  ( $B = \text{Al}^{3+}_{0.5}\text{Si}_{0.5}$ ) octahedra. Yellow spheres are oxygen, blue spheres are  
 308  $\text{Si}/\text{Al}^{3+}$ , and red spheres are  $\text{Mg}/\text{Fe}^{3+}$ .



309

310 **FIGURE 3.** Goldschmidt diagram for selected  $ABO_3$  perovskite and the  $LN$ -type compounds (yellow  
 311 shading). Dotted lines are contours of the Goldschmit tolerance factor. Open symbols: perovskite-forming  
 312 compounds ( $CaSiO_3$ ; Liu and Ringwood, 1975;  $MgSiO_3$ ; Ito and Matsui, 1978). Solid symbols:  $LN$ -type  
 313 quenched products,  $(Mg_{0.5}Fe^{3+}_{0.5})(Si_{0.5}Al_{0.5})O_3$  (this study),  $Mg_{0.75}Al_{0.25}Si_{0.75}O_3$  (Liu et al., 2016, 2017a;  
 314 Ishii et al., 2017),  $FeTiO_3$  (Akaogi e al., 2016),  $MnTiO_3$  (Ko and Prewitt, 1988), and  $LiNbO_3$  (Megaw,  
 315 1968).





316  
 317 **FIGURE 4.** Ternary phase diagram of the  $(\text{Mg}, \text{Fe}^{2+})\text{O}-\text{Fe}^{3+}\text{AlO}_3-\text{SiO}_2$  system for showing the  
 318 compositions of Fe and Al-bearing bridgmanite in previous and present studies. The grey shadow is the  
 319 magnified region from the whole ternary phase relations. The black star represents the composition of  
 320 pyrolite by assuming the amount of  $\text{Fe}^{3+}/\Sigma\text{Fe}$  of 50-60% under the reduced conditions (McCammon,  
 321 1997; Frost and Langenhorst, 2002), while the square represents that of MORB. Abbreviation: CCS,  
 322 charge-coupled substitution ( $\text{Mg}^{2+} (\text{A}) + \text{Si}^{4+} (\text{B}) = \text{M}^{3+} (\text{A}) + \text{M}^{3+} (\text{B})$ , where M represent  $\text{Fe}^{3+}$  or  $\text{Al}^{3+}$ );  
 323 OVS, oxygen vacancy substitution ( $2 \text{Si}^{4+} (\text{B}) + \text{O}^{2-} = 2\text{M}^{3+} (\text{B}) + \text{V}_\text{o}$ , where  $\text{V}_\text{o}$  is the oxygen vacancy).

324  
 325  
 326  
 327  
 328  
 329  
 330  
 331  
 332